

A microscopic model of electron transport in quantum dot infrared photodetectors

Nenad Vukmirović^{a)}, Zoran Ikonić, Ivana Savić, Dragan Indjin, and Paul Harrison

*School of Electronic and Electrical Engineering,
University of Leeds, Leeds LS2 9JT, United Kingdom*

Abstract

A theoretical model describing the electron transport in vertical conductivity quantum dot infrared photodetectors is presented. The carrier wave functions and energy levels were evaluated using the strain dependent 8-band $k \cdot p$ Hamiltonian and used to calculate all intra- and inter-period transition rates due to interaction with phonons and electromagnetic radiation. The interaction with longitudinal acoustic phonons and electromagnetic radiation was treated perturbatively within the framework of Fermi's golden rule, while the interaction with longitudinal optical phonons was considered taking into account their strong coupling to electrons. A system of rate equations was then formed, from which the macroscopic device output parameters like dark current and responsivity, as well as microscopic information about carrier distribution in quantum dots and continuum states, could be extracted. The model has been applied to simulate the dark current, as well as the mid-infrared photoresponse in an experimentally realized device [J. Appl. Phys. **89**, 4558 (2001)] and a good agreement with experiment has been obtained. Being free from any fitting or phenomenological parameters, the model should be a useful tool in the design and prediction of the characteristics of the existing or new types of quantum dot infrared photodetectors.

^{a)} Electronic mail: eennv@leeds.ac.uk

I. INTRODUCTION

In the last decade, quantum dot infrared photodetectors (QDIPs),¹⁻⁸ utilizing electron intraband transitions to detect incident infrared radiation, have emerged as an alternative technology aiming to replace quantum well and HgCdTe infrared detectors. The expected advantages of QDIPs are their inherent sensitivity to normal-incidence radiation, high operating temperature and low dark current. In(Ga)As/GaAs quantum dots grown on GaAs substrate,^{1-4,8-18} being probably the most explored quantum dot material system, are typically used in QDIPs, however other material systems have also attracted attention such as InAs quantum dots grown on InP,⁷ InGaAs/InGaP dots grown on GaAs substrate,¹⁹⁻²¹ InAs/InAlAs dots grown on InP,²² GaN/AlN²³ and Ge/Si quantum dots.²⁴ QDIP devices utilize two different geometries - lateral conductivity QDIPs and vertical conductivity QDIPs.²⁵ Vertical QDIPs have been the subject of more intensive research due to their suitability for application as focal plane arrays,^{5,6} although lateral QDIPs have demonstrated excellent performance too.²⁵

The afore mentioned experimental work has initiated the development of several theoretical approaches with different level of complexity to understand the performance of QDIPs. As the detection is based on the process of absorption of incident radiation, a significant amount of theoretical work was focused on calculation of the intraband optical matrix elements within the one band effective mass approach^{15,26-29} or the 8-band $k \cdot p$ method.³⁰ Some theoretical efforts have also been made to model the current under dark or light conditions.^{9,31-37} In these models, the current is deduced from the analysis of the processes of carrier capture, thermal escape and photoexcitation. However, the rates of these processes are calculated using parameters that were either taken phenomenologically, deduced from experiment, or obtained by fitting. None of these models aims to predict the dependence of relevant QDIP output parameters, such as responsivity or dark current on the choice of material system used or on quantum dot size and composition, which it is highly desirable to know in order to optimize QDIP characteristics. Deeper understanding of underlying QDIP physics can also be achieved by obtaining information about carrier distribution among various quantum dot and continuum energy levels, which is hardly to access experimentally.

In this work, we therefore present a theoretical model of vertical electron transport in quantum dot infrared photodetectors. The model starts from the energy level and wave

functions calculation, followed by evaluation of transition rates between all pairs of states, from which a system of nonlinear rate equations is formed. From its steady state solution in dark or light conditions, the population of energy levels and consequently the dark current and responsivity are calculated. The details of the model are presented in Sec. II, while the results obtained by its application to one of the reported InAs/GaAs QDIP structures¹⁴ are given in Sec. III.

II. THEORETICAL MODEL

QDIPs consist of periodically arranged layers of quantum dots (see Fig. 1a), with the period typically equal to $L_z = 50\text{nm}$ chosen to minimize the dark current channel via transport between bound states of quantum dots in neighboring periods. At such a value of quantum dot period, the quantum dots are not vertically aligned, and the whole structure is not strictly periodic in the z -direction. Nevertheless, as a reasonably good approximation, the vertical arrangement and the periodicity of the structure will be assumed in the model as shown in Fig. 1b. The processes that determine the dark and light current are the excitation of carriers from the bound quantum dot states to resonant continuum states mainly localized in the quantum dot region, their subsequent transport via the continuum states to the next period, and possible capture of carriers from the continuum by quantum dots, but not the direct transport between quantum dot bound states of neighboring periods. Therefore, it is not expected that the transport properties of QDIPs are dependent on the details of the quantum dot arrangement, hence the simplest possible periodic arrangement is chosen in the model.

In order to prevent high values of dark current, quantum dots used in QDIPs are typically either doped at a relatively low level to populate just the ground state or undoped. It is therefore reasonable to assume a uniform electric field throughout the structure as the formation of electric field domains^{38,39} is expected to occur only at high doping densities.

A. Modelling the electronic structure

The energy states of a quantum dot superlattice subjected to a uniform electric field possess the property of shift-invariance. For each state assigned to a certain period of the

superlattice (called the central period in the text), there is a set of corresponding states obtained by translating the wave function in the growth direction by multiples of the superlattice period. The corresponding eigenenergies are shifted by multiples of the potential drop due to electric field over one period (see Fig. 2). Therefore, it is enough to find the energy levels assigned to one period only, and the others are then obtained by exploiting the shift-invariance property. The states assigned to the central period are obtained by solving the Hamiltonian eigenvalue problem in the region of space containing $2N + 1$ periods (central period, N periods to the left and N periods to the right) and selecting only the eigenstates whose probability of finding a carrier in the central period is larger than in any of the other $2N$ periods. In the calculations, a value of $N = 2$ was taken based on large value of superlattice period compared to quantum dot size and previous experience with simulations of quantum well infrared photodetectors.^{40,41}

The 8-band strain dependent $k \cdot p$ Hamiltonian⁴² is used to model the single-particle states in the conduction band. The strain distribution was modeled using the continuum mechanical model^{43,44} and was found using the finite element method on a rectangular nonuniform grid where first order Lagrange interpolation elements were used.⁴⁵ Due to the periodicity of the structure, periodic boundary conditions in the growth direction were imposed, therefore the strain tensor components need to be found in a single period only. It was assumed that the dot shape is cylindrically symmetric as most dots in experimentally realized QDIPs exhibit such shape. The axial approximation then allows us to reduce the problem from three dimensional to two dimensional.⁴⁶ The cylindrical symmetry of the dots then introduces a good quantum number of the z -component of the total angular momentum m_f (where m_f is half integer). The orthonormal wave function expansion method was used to find the eigenenergies and the corresponding wave functions. The method is based on assuming each of the eight envelope wave functions as a linear combination of the expansion basis functions

$$\psi_i(\mathbf{r}) = \sum_{nl} A_{inl} b_{nm(i)l}(r, z, \varphi), \quad (1)$$

with the coefficients A_{inl} ($i \in \{1, \dots, 8\}$, $n \in \{1, \dots, n_{max}\}$ and $l \in \{-l_{max}, \dots, l_{max}\}$) to be determined, where $m(i) = m_f - m_j(i)$ and $m_j(i)$ is the eigenvalue of the z -component of the total angular momentum of the Bloch function $|i\rangle$ (its explicit values for one choice of the Bloch function basis can be found for example in Ref. 47). The basis functions b_{nml} are

given by

$$b_{nml}(r, z, \varphi) = f_{nm}(r)g_l(z)\Phi_m(\varphi), \quad (2)$$

where

$$\begin{aligned} f_{nm}(r) &= \frac{\sqrt{2}}{R_t} \frac{J_m(k_{nm}r)}{|J_{|m|+1}(k_{nm}R_t)|}, \\ g_l(z) &= \frac{1}{\sqrt{H_t}} e^{i\frac{2\pi}{H_t}lz}, \\ \Phi_m(\varphi) &= \frac{1}{\sqrt{2\pi}} e^{im\varphi}, \end{aligned} \quad (3)$$

where l and m are integers and n is a positive integer, R_t and H_t are the radius and the length of the region of space in which the Hamiltonian eigenvalue problem is solved (see Fig. 3), J_m is a Bessel function of order m , and $k_{nm}R_t$ is its n -th zero. After substituting Eq. (1) into Hamiltonian eigenvalue problem one can derive the corresponding Hamiltonian matrix. The eigenvalues of this matrix are in fact the energies and its eigenvectors contain the coefficients in the wave function expansion.

B. Carrier interaction with phonons and electromagnetic radiation

Due to the discrete nature of states in quantum dots, transition rates between electronic states due to interaction with longitudinal optical (LO)-phonons have previously been considered to be vanishingly small unless the energy levels are separated by the energy of an LO-phonon.⁴⁸ Furthermore, longitudinal acoustic (LA)-phonons, due to their small energy, cause transitions only between closely spaced energy levels. These expectations led to the predictions of extremely low dark currents and very small capture rates in QDIPs due to inhibited carrier dynamics. Consequently excellent QDIP characteristics were expected. However, it is currently thought that the electron-LO-phonon interaction in quantum dots cannot be taken into account within the framework of first order perturbation theory and should be considered in the strong coupling regime,^{49,50} when the entangled electron-LO-phonon states called polarons are formed. The polaron dynamics are then determined by the decay of the LO-phonon part of the polaron to two LA-phonons.^{51,52} Therefore, full modeling of the carrier dynamics would require the calculation of the polaronic, rather than electronic structure only, which would be computationally very demanding. Nevertheless, as the polaron states still remain mainly electronic or phononic,^{52,53} the electronic states found

using the method presented in Sec. II A closely resemble the mainly electronic polaron states. The transition rate between such states due to the interaction with an LO-phonon and its subsequent decay to two LA-phonons are calculated using the approach that was introduced in Ref. 51. Subsequently it was used to model the experimental results on intraband carrier dynamics in quantum dots^{54,55} and in the feasibility study of intraband quantum dot lasers.^{53,56} The transition rate from the initial state with an electron in state i (with energy E_i) to the final state with an electron in state f (with energy E_f) and one more (less) phonon is therefore given by^{51,56}

$$W_{if} = \Gamma - \frac{\sqrt{2(R - X)}}{\hbar}, \quad (4)$$

where $R = \sqrt{X^2 + Y^2}$, $X = g^2 + (\Delta_{if}^2 - \Gamma^2 \hbar^2)/4$, $Y = \Gamma \hbar \Delta_{if}/2$, $\Delta_{if} = E_i - E_f \mp \hbar \omega_{LO}$, $\hbar \omega_{LO}$ is the LO-phonon energy, Γ is the inverse LO-phonon lifetime due to its decay into two LA-phonons, $g^2 = \sum_{\mathbf{k}} |g_{\mathbf{k}}|^2$ is the electron-LO-phonon coupling strength, which under the assumption of bulk LO-phonon modes and the Frölich interaction Hamiltonian reads⁵⁶

$$g^2 = \sum_{\mathbf{k}} (n_{LO} + 1/2 \pm 1/2) |\alpha(\mathbf{k})|^2 |F_{if}(\mathbf{k})|^2, \quad (5)$$

where n_{LO} is the phonon occupation number and

$$|\alpha(\mathbf{q})| = \frac{1}{q} \sqrt{\frac{e^2 \hbar \omega_{LO}}{2V} \left(\frac{1}{\varepsilon_{\infty}} - \frac{1}{\varepsilon_{st}} \right)}, \quad (6)$$

with V being the volume of the embedding cylinder, ε_{∞} and ε_{st} the high frequency and static dielectric constants, respectively, and where

$$F_{if}(\mathbf{q}) = \sum_{j=1}^8 \int_V d^3 \mathbf{r} \psi_j^{(f)}(\mathbf{r})^* e^{i\mathbf{q}\cdot\mathbf{r}} \psi_j^{(i)}(\mathbf{r}) \quad (7)$$

is the electron-phonon interaction form-factor. The envelope functions of the initial and final state are given as

$$\psi_j^{(i)}(\mathbf{r}) = \sum_{nl} A_{jnl}^{(i)} b_{nm(j)l}(r, z, \varphi), \quad (8)$$

$$\psi_{j'}^{(f)}(\mathbf{r}) = \sum_{n'l'} A_{j'n'l'}^{(f)} b_{n'm'(j')l'}(r, z, \varphi), \quad (9)$$

where $m(j) = m_f - m_j(j)$ and $m'(j') = m'_f - m_j(j')$ with m_f and m'_f being the z -components of the total angular momentum of the initial and final state, respectively. One of the very convenient features of the wave function expansion method is that the form factor, Eq. (7),

can be evaluated without the numerically demanding three dimensional integration. Instead, after substituting Eqs. (8) and (9) into Eq. (7) one finds that it can be expressed in terms of the expansion coefficients as

$$F_{if}(\mathbf{q}) = \sum_{j=1}^8 \sum_{nl, n'l'} A_{jnl}^{(i)*} A_{jn'l'}^{(f)} f_1(q_z, \Delta l) \times f_2(m_f, m'_f, n, n', q_r, j), \quad (10)$$

where

$$f_1(q_z, \Delta l) = \frac{1}{H_t} \frac{e^{i(q_z + \frac{2\pi}{H_t} \Delta l) H_t/2} - e^{-i(q_z + \frac{2\pi}{H_t} \Delta l) H_t/2}}{i(q_z + \frac{2\pi}{H_t} \Delta l)} \quad (11)$$

is an analytic function of its arguments, while

$$f_2(m_f, m'_f, n, n', q_r, j) = \frac{1}{2\pi} \int_0^{2\pi} d\varphi \int_0^{R_t} r dr e^{i\Delta m_f \varphi} \times e^{i(q_x \cos \varphi + q_y \sin \varphi)r} f_{nm(j)}(r) f_{n'm'(j)}(r), \quad (12)$$

where $\Delta l = l' - l$, $\Delta m_f = m'_f - m_f$, and

$$q_r = \sqrt{q_x^2 + q_y^2}.$$

The function f_2 does not depend on the wave functions and can be tabulated once for all arguments before evaluating the form factors. Finally, since $F_{if}(\mathbf{q})$ depends on the radial and the z -component of the wave vector only (and not on the φ -component), the summation (integration) over \mathbf{q} in Eq. (5) can be simplified from three dimensional to two dimensional.

The weaker electron-LA-phonon scattering was calculated using Fermi's Golden rule. The transition rate from an initial state i to a final state f is then given by^{55,56}

$$W_{if} = \Theta[\pm(E_i - E_f)] (n_{\mathbf{q}_s} + 1/2 \pm 1/2) \frac{D_A^2 q_s^3}{\hbar \rho v_s^2} \times \int \sin \theta_q d\theta_q d\varphi_q |F_{if}(\mathbf{q}_s)|^2, \quad (13)$$

where D_A is the acoustic phonon deformation potential, ρ the density and v_s the longitudinal sound velocity, $q_s = |E_i - E_f|/(\hbar v_s)$, $n_{\mathbf{q}_s}$ is the number of LA-phonons with wave vector \mathbf{q}_s , $\Theta(x)$ is the step function and (θ_q, φ_q) are the spherical coordinates of the vector \mathbf{q}_s . The linear and isotropic acoustic phonon dispersion relation $\omega(\mathbf{q}) = v_s q$ is assumed. Since the form factor does not depend on φ_q , the two dimensional integration in Eq. (13) can be reduced to one dimensional.

Other possible types of scattering were not included in the calculation and we now discuss the reasons for that. As in QDIP operating conditions, only the ground state is significantly populated and the populations of the wetting layer and the continuum states are small; all the processes originating from the Coulomb interaction among carriers, being proportional to the carrier density, can therefore be neglected. These are, for example, the relaxation of bound states assisted by the Coulomb interaction between bound and wetting layer carriers,^{57,58} or the Coulomb scattering among the carriers in the continuum or wetting layer. Coulomb scattering between bound states is also suppressed as in a system with discrete energy levels it is difficult to achieve the resonance imposed by the condition of energy conservation.⁵⁶ This is also the case for ionized impurity scattering in the case of structures with a doped active region, although in this work the structure with an undoped active region was considered. We have previously shown⁵⁶ that the relaxation rates due to spontaneous emission of photons are much smaller than the other relaxation rates in the system. Finally, in the realistic device, some number of defects is present, depending on the quality of growth. The defects are another potential source of scattering, and as they are not included in the model, it is expected that the results of the model should be valid in the limit of high-quality samples with low defect density.

The interaction with incident electromagnetic radiation was treated in a standard manner^{56,59} within the dipole approximation and Fermi's golden rule. The optical cross section of the $i \rightarrow f$ transition due to absorption of electromagnetic radiation of angular frequency ω is then given by⁵⁶

$$\sigma_{if}^{\varepsilon}(\omega) = \frac{2\pi}{\bar{n}\varepsilon_0 c \omega} |\mathcal{M}_{if}^{\varepsilon}|^2 g(E_f - E_i - \hbar\omega, 2\sigma), \quad (14)$$

where \bar{n} is the refraction index, and E_f and E_i are the energies of the final and the initial state, respectively. $\mathcal{M}_{if}^{\varepsilon} = \langle i | \hat{H}' | f \rangle / A$ is the perturbation matrix element which depends only on the direction ε of light polarization and not on the amplitude of A . The inhomogeneous broadening due to size inhomogeneity of the quantum dot ensemble was taken into account by replacing the delta function in Fermi's golden rule with a Gaussian given by

$$g(x, 2\sigma) = \frac{1}{\sigma\sqrt{2\pi}} \exp\left(-\frac{x^2}{2\sigma^2}\right). \quad (15)$$

In a similar manner as the form factors, the absorption matrix elements can be expressed

in terms of the expansion coefficients as

$$\mathcal{M}_{if}^\varepsilon = \sum_{jnl} \sum_{j'n'l'} A_{jnl}^{(i)*} A_{j'n'l'}^{(f)} G(jnl, j'n'l'), \quad (16)$$

where the perturbation Hamiltonian matrix elements are

$$G(jnl, j'n'l') = \frac{1}{A} \int_V d^3\mathbf{r} b_{nm(j)l}^* \hat{H}' b_{n'm(j')l'}. \quad (17)$$

The cylindrical symmetry of the dots introduces the following selection rules: $\Delta m_f = 0$ for z -polarized radiation and $|\Delta m_f| = 1$ for in-plane polarized radiation.

C. The transport model

The energy levels of a quantum dot superlattice will be denoted as $i = (M, P)$ representing the P -th level in ascending order of energies among the levels belonging to the period M . The populations of energy levels and the current in the device will be found from the semiclassical (Boltzmann equation) model, which due to the discreteness of the energy levels reduces to the following system of rate equations:

$$\begin{aligned} \frac{dn_i}{dt} = & \sum_{j \neq i} W_{ji} n_j \left(1 - \frac{1}{2} n_i\right) - \sum_{j \neq i} W_{ij} n_i \left(1 - \frac{1}{2} n_j\right) - \\ & - \sum_j \sigma_{ij}^p(\omega) (n_i - n_j) \Phi, \end{aligned} \quad (18)$$

where $0 \leq n_i \leq 2$ is the occupancy of level i including electrons of both spin, W_{ij} is the total transition rate from state i to state j due to interaction with phonons, $\sigma_{ij}^p(\omega)$ is the optical cross section between states i and j for incident radiation of angular frequency ω and polarization p and Φ is the flux of incident radiation. The effect of final state blocking is included via the terms $(1 - n_i/2)$ that represent the probability that the final state is empty.

Due to the periodicity of the structure the relations

$$\begin{aligned} n_{(M,P)} &= n_{(L,P)}, \\ W_{(M,P),(L,Q)} &= W_{(M+K,P),(L+K,Q)}, \\ \sigma_{(M,P)(L,Q)} &= \sigma_{(M+K,P)(L+K,Q)} \end{aligned} \quad (19)$$

hold.^{40,41,60} After exploiting them, the system of equations (18) is reduced and contains only the occupations of levels assigned to a central period. Furthermore, in the spirit of the nearest

neighbors approximation, introduced in Sec. II A, only the transitions with $|M - L| \leq N$ are considered. As usual, the system of rate equations should be supplemented by the condition imposing the total number of particles in the system. It is therefore assumed that there are n_d electrons per quantum dot on the average, i.e. $\sum_P n_{(M,P)} = n_d$. In order to obtain a finite system of equations, one also has to limit the number of levels per period, i.e. take into account only the states with $P < P_{\max}$. It has been checked for each field that the number of states taken in the calculation was sufficient.

As the carrier transition rates in QDIPs are much smaller than the frequencies of external excitations, one is mainly interested in the steady-state response ($d/dt = 0$). Nevertheless, the rate equations are solved by time integration of the system of equations (18), starting from an initial condition that all carriers are in the ground state and performing the integration until the steady state is reached. Such a method is extremely reliable in terms of convergence unlike the methods for solving a large system of nonlinear equations.⁶¹

After the system of equations (18) is solved, the current in steady-state conditions is found by selecting a certain reference plane normal to the growth direction and keeping track of the amount of charge that passes through that plane in a unit of time. Let p_i be the probability that the electron in state i is located to the left of the reference plane. The contribution to the current from the transitions from level i to level f is then given by

$$J_{if} = -e(W_{if} + \sigma_{if}\Phi) n_i \left(1 - \frac{n_f}{2}\right) \times [p_i(1 - p_f) - p_f(1 - p_i)]. \quad (20)$$

The first term in square brackets in Eq. (20) accounts for the carriers that were initially on the left side of the reference plane and pass to the right side, while the second term considers the carriers that were on the right and pass to the left and clearly gives the contribution to current of an opposite sign to the previous one. The total current is calculated by adding the contributions of the current from all the transitions considered.

The probability of finding an electron whose wave function is given by Eq. (1) in a region of space $a \leq z \leq b$

$$p = \int_{a \leq z \leq b} d^3\mathbf{r} \sum_{i=1}^8 |\psi_i(\mathbf{r})|^2 \quad (21)$$

can also be expressed in terms of the expansion coefficients as

$$p = \sum_{nl'} \sum_i A_{inl}^* A_{inl'} \int_a^b dz g_l(z)^* g_{l'}(z), \quad (22)$$

where the last integral is evaluated analytically. This expression is used both for the current calculation according to Eq. (20) and assigning a certain period to the state as described in Sec. II A.

III. RESULTS

The model presented in Sec. II has been applied to the simulation of the InAs/GaAs QDIP structure reported in Ref. 14 (the structure labeled as S-GaAs therein). Quantum dots are assumed to be of conical shape with the diameter $D = 25$ nm and height $h = 7$ nm which are approximately the reported dimensions of the dots. A wetting layer with the width of $d_{\text{WL}} = 0.5$ nm is considered as well. The same set of material parameters for the InAs/GaAs material system as in Ref. 56 was taken.

The calculated energy levels, as well as the effective potential profile on the z -axis for the analyzed structure subjected to the electric field $F = 10$ kV/cm are shown in Fig. 2. Due to relatively large size of the dots, there is a significant number of bound energy levels. The ground state is strongly bound and positioned 300 meV below the continuum in agreement with the experimental results obtained from photoluminescence and photoluminescence excitation studies.¹⁴ The ground state has the z -component of total angular momentum $|m_f| = 1/2$, while the other bound states have $|m_f| \leq 9/2$ and are shown in Fig. 4. The calculations have shown that the change in the energy level structure of the bound states with electric field is small and therefore the structure shown in Figs. 2 and 4 can be considered to be a typical representative of the position of energy levels for any field. It can be seen that the states are grouped into five groups according to their energies with energy gaps in between. While the model presented in Sec. II treats all the states on equal footing regardless of whether such grouping occurs or not, the groups will be labeled with G_1 - G_5 and will be used in the discussion to build an intuitive picture of the microscopic processes in the device.

A. The dark conditions

The calculated dark current density–electric field characteristics at three different temperatures is given in Fig. 5. For comparison with experimental results where current voltage

characteristics are reported, a mesa area of $A = 5 \cdot 10^{-4} \text{ cm}^2$ in accordance with the reported mesa diameter of $250 \mu\text{m}$ is assumed, and the uniform electric field distributed along the 340 nm long structure is taken. A realistic quantum dot density of $6 \cdot 10^{10} \text{ cm}^{-2}$ is taken and it is assumed that there are $n_d = 1$ electrons per dot on average, which is a typical quantum dot occupation number in the case when relatively small voltages are applied in $n^+ \text{-i-n}^+$ structures.⁶² The comparison with the experiment should be taken with caution as the reported QDIP structure consists of 5 periods only and it is possible that the effects of contacts, not taken into account in our model of the periodic structure, might become important in such cases. Nevertheless, one certainly expects the same trends and at least the same order of magnitude of dark current. The inset in Fig. 5 shows that an overall good agreement between the theoretical and experimentally measured results at $T = 77 \text{ K}$ is found, especially bearing in mind that the current changes by seven orders of magnitude in the range of electric fields investigated. It can also be seen that the expected exponential increase of current with field, followed by its saturation is obtained, as well as an increase of current with temperature. The microscopic origin of these expected results will be presented in what follows.

The carrier distribution among various energy levels at $T = 77 \text{ K}$ is shown in Fig. 6. At small values of the electric field the carriers appear to be thermalized and the distribution resembles the equilibrium one. Most of the carriers are then in the ground state. At medium fields the majority of carriers still remain in the ground state, however the nonequilibrium distribution becomes clearly evident with some of the continuum states being more populated than certain bound states. Finally, large values of the electric field significantly increase the population in the continuum and at the same time the occupancy of the ground state falls. The effect of temperature (at a fixed electric field) on the carrier population is similar to the effect of electric field – larger temperatures promote more carriers to the continuum and eventually deplete the ground state.

In order to identify the main carrier transport channels causing the presence of carriers in the continuum and consequently the dark current in the device, the transition rates between different quantum dot states are analyzed. The main transition mechanism is due to interaction with LO-phonons, while the interaction with LA-phonons that carry only a small amount of energy ($\lesssim 5 \text{ meV}$) mainly causes the redistribution of carriers within the same group of states, but cannot cause transitions between states from different groups. In

order to participate in current, the carriers must eventually be excited to the continuum (group G_5 , see Fig. 4) states. The carriers are naturally in the ground (G_1 group) state and only the excitations such as temperature and higher electric fields can populate higher states.

At low values of electric field, the main carrier route to the continuum is via a sequence of transitions $G_1 \rightarrow G_2$, $G_2 \rightarrow G_3$, $G_3 \rightarrow G_4$ and finally $G_4 \rightarrow G_5$. The transitions between non-adjacent groups of bound states, (such as $G_1 \rightarrow G_3$, $G_1 \rightarrow G_4$ or $G_2 \rightarrow G_4$), as well as direct excitations to G_5 states are much less probable due to the larger energy difference (and hence the smaller transition rates) between the levels. When the electric field is increased, the continuum states from the left neighboring periods (Fig. 2) start to penetrate the quantum dots of the central period. As the field increases the energy of these states decreases and the overlap with the bound states of the central period increases, providing additional channels for carrier excitation to the continuum states. This firstly affects the transition rate from G_4 to G_5 , as shown in Fig. 7, which increases since the carriers can now be excited not only to the continuum states assigned to the central period, but also to the continuum states of the neighboring periods with smaller energy distance from G_4 and the overlap which is still sufficient to increase the transition rates. As the electric field is further increased, additional paths of direct carrier excitation to the continuum, such as G_3 to G_5 , and at larger fields even G_2 to G_5 , are opened and the dark current is therefore significantly increased.

The influence of temperature on the carrier excitation into the continuum is more transparent. The transition rates to higher states in all the paths mentioned, being proportional to the number of LO-phonons, increase with temperature (as seen for example from Fig. 7) and therefore the number of carriers excited to the continuum and the dark current increase.

B. The light conditions

The results of the simulation of the mid-infrared (100–250 meV) optical response of the structure investigated, are now presented. Under normal QDIP operating conditions the carriers are mostly in the ground state, and the main origin of the optical response is the absorption of carriers from the ground state. In agreement with previous theoretical and experimental results,^{13,15,26} the calculation shows that significant absorption of the in-plane polarized radiation from the ground state may occur only on transitions to G_2 states and is

located in the far-infrared region. The transitions in the mid-infrared region may therefore only be due to z -polarized radiation and from here we only address the transitions due to this polarization. The energy dependence of the optical matrix elements for the absorption of z -polarized radiation from the ground state at an electric field of $F = 10 \text{ kV/cm}$ is shown in Fig. 8. It can be also considered as the representative graph for any value of the electric field, as the dominant bound to bound transition matrix elements are weakly influenced by the operating bias. The carriers from the ground state are mainly absorbed to the state of the same symmetry from the G_4 group and to a smaller extent to the state from the G_3 group.

The QDIP responsivity at the angular frequency of incident radiation ω is defined as

$$R(\omega) = \frac{J(\Phi) - J(\Phi = 0)}{\hbar\omega\Phi}. \quad (23)$$

In the simulation, the standard deviation of the Gaussian linewidth due to size inhomogeneity of the quantum dot ensemble was taken to be equal to 10% of the transition energy, which is approximately the experimental value of the dominant transition in Ref. 14. The spectral responsivity curves at several different values of the electric field and a temperature of $T = 77 \text{ K}$ are presented in Fig. 9. All of them exhibit a main peak around 180 meV originating from the absorption from the ground state to the state from the G_4 group, while at higher values of the electric field another peak at an energy around 115 meV occurs, due to a transition to the state from the G_3 group. The positions of the peaks are in agreement with experiment¹⁴ where the strong peak at 175 meV is accompanied by the weaker one at 115 meV. The peak responsivity mainly increases with electric field as one might expect, but at large values of the electric field it starts to drop. These features can be understood as follows. The carriers that are absorbed from the ground to a state from the G_4 group need to be promoted to the continuum to cause photocurrent. The transition rate from G_4 to the continuum states increases with field, as already explained in Sec. III A and shown in Fig. 7, causing the photocurrent to increase. However at larger values of electric field the population of the ground state falls (see Fig. 6), therefore there are less carriers that can be absorbed, causing the photocurrent to decrease, see Fig. 9. The smaller peak due to absorption to the G_3 state is not present at low fields due to the small probability of further promotion of carriers from the G_3 states to the continuum. At larger fields, when the transition path $G_3 \rightarrow G_5$ is activated (Fig. 7), this peak starts to appear.

The spectral responsivity curves for different temperatures at two values of electric field are given in Fig. 10. The influence of temperature on the responsivity can be understood in a similar manner as the influence of electric field. At smaller values of electric field, the responsivity increases with temperature, as the carriers absorbed to the state from G_4 group are more likely to be promoted to the continuum at higher temperatures. On the other hand, at larger values of the electric field when the ground state starts to be depleted, higher temperature additionally reduces the number of carriers in the ground state, causing less carriers to be absorbed from the ground state and consequently a smaller photocurrent.

It is more difficult to give a fair comparison of the theoretical and experimental responsivity results than in the case of the dark current. In the model, an ideally z -polarized excitation, performing a single pass through the QDIP active region, is considered. The experiment reported in Ref. 14 was performed in normal incidence geometry, when the incident radiation is certainly not ideally z -polarized and a quantitative comparison of the actual value of the responsivity would require a more detailed analysis of the coupling of the optical field with the active region of the QDIP structure. It can still be said that our results for the responsivity of the order of $R \sim 1$ A/W are consistent with the experimental results. Indeed, from the photocurrent spectra and optical excitation power reported in Ref. 14, one may estimate the experimental responsivity to be of the order $R \sim (0.1 - 1)$ A/W for different values of voltage. Furthermore, the simulation also predicts a fall of responsivity at higher voltages, as observed in the experiment. The temperature of $T = 77$ K was identified in the experiment as optimal temperature in terms of the maximization of the responsivity. In the simulation the responsivity at low voltages increases with temperature, and at high voltages decreases with temperature, one should therefore expect that there is an intermediate region where it exhibits a nonmonotonic behavior. However, for none of the values of the electric field used in simulation was such behavior observed, implying that the simulation probably predicts a steeper transition between the two regimes than it is in reality.

A further insight into the origin of the photocurrent can be obtained by analyzing the distribution of the photoexcited carriers. The difference between the state occupancies under light and dark conditions for three values of the electric field at $T = 77$ K is given in Fig. 11. At a field of $F = 5$ kV/cm, most of the carriers photoexcited to G_4 states relax back to the lower states, rather than escaping into the continuum. The carriers absorbed from the ground state are then distributed among G_2 - G_4 states. At a higher field of $F =$

15 kV/cm, the carriers photoexcited to G_4 have a significant probability to make a transition to the continuum states. Most of the carriers absorbed from the ground state are therefore distributed among continuum levels, as can be seen from Fig. 11. The same also holds for the field of $F = 30$ kV/cm, but due to a drop in the occupation of the ground state under dark conditions, the total number of absorbed carriers is smaller than at $F = 15$ kV/cm.

IV. CONCLUSION

In conclusion, a microscopic model of the electronic transport in vertical conductivity QDIPs was developed. The model considers the transitions between various quantum dot bound and continuum states to evaluate the current under dark or light conditions, without resorting to any fitting parameters. The model was applied to one of the experimentally reported QDIP structures. A very good agreement with the dark current experimental results was found in the range of voltages where the current changes as much as seven orders of magnitude. The simulations also predict most of the experimentally observed trends in responsivity.

The proposed model should therefore serve as a useful tool in the analysis of the characteristics of existing QDIP devices, providing a better understanding of their performance and enabling researchers to find the way for possible device improvements. More importantly, as the model does not contain any fitting parameters, it can be used to predict the performance of new types of QDIP devices and suggest whether such devices would perform better than the existing ones. Finally, the model gives a deeper insight into internal QDIP physics, extracting important information about carrier excitation paths to the continuum and carrier distribution both under dark and light conditions.

-
- ¹ D. Pan, E. Towe, and S. Kennerly, *Appl. Phys. Lett.* **73**, 1937 (1998).
- ² S. Maimon, E. Finkman, G. Bahir, S. E. Schacham, J. M. Garcia, and P. M. Petroff, *Appl. Phys. Lett.* **73**, 2003 (1998).
- ³ E. T. Kim, Z. H. Chen, and A. Madhukar, *Appl. Phys. Lett.* **79**, 3341 (2001).
- ⁴ L. Fu, P. Lever, K. Sears, H. H. Tan, and C. Jagadish, *IEEE Electron Dev. Lett.* **26**, 628 (2005).
- ⁵ J. Jiang, K. Mi, S. Tsao, W. Zhang, H. Lim, T. O’Sullivan, T. Sills, M. Razeghi, G. J. Brown, and M. Z. Tidrow, *Appl. Phys. Lett.* **84**, 2232 (2004).
- ⁶ S. Krishna, D. Forman, S. Annamalai, P. Dowd, P. Varangis, T. Tumolillo, A. Gray, J. Zilko, K. Sun, M. G. Liu, et al., *Appl. Phys. Lett.* **86**, 193501 (2005).
- ⁷ W. Zhang, H. Lim, M. Taguchi, S. Tsao, B. Movaghar, and M. Razeghi, *Appl. Phys. Lett.* **86**, 191103 (2005).
- ⁸ C. Kammerer, S. Sauvage, G. Fishman, P. Boucaud, G. Patriarche, and A. Lemaître, *Appl. Phys. Lett.* **87**, 173113 (2005).
- ⁹ A. D. Stiff-Roberts, X. H. Su, S. Chakrabarti, and P. Bhattacharya, *IEEE Photonics Technol. Lett.* **16**, 867 (2004).
- ¹⁰ Z. Ye, J. C. Campbell, Z. Chen, E.-T. Kim, and A. Madhukar, *J. Appl. Phys.* **92**, 7462 (2002).
- ¹¹ G. Ariyawansa, A. G. U. Perera, G. S. Raghavan, G. von Winckel, A. Stintz, and S. Krishna, *IEEE Photonics Technol. Lett.* **17**, 1064 (2005).
- ¹² A. M. Adawi, E. A. Zibik, L. R. Wilson, A. Lemaître, J. W. Cockburn, M. S. Skolnick, M. Hopkinson, and G. Hill, *Appl. Phys. Lett.* **83**, 602 (2003).
- ¹³ L. Rebohle, F. F. Schrey, S. Hofer, G. Strasser, and K. Unterrainer, *Appl. Phys. Lett.* **81**, 2079 (2002).
- ¹⁴ Z. Chen, O. Baklenov, E. T. Kim, I. Mukhametzhanov, J. Tie, A. Madhukar, Z. Ye, and J. C. Campbell, *J. Appl. Phys.* **89**, 4558 (2001).
- ¹⁵ F. F. Schrey, L. Rebohle, T. Müller, G. Strasser, K. Unterrainer, D. P. Nguyen, N. Regnault, R. Ferreira, and G. Bastard, *Phys. Rev. B* **72**, 155310 (2005).
- ¹⁶ S. Sauvage, P. Boucaud, T. Bruhnes, V. Immer, E. Finkman, and J. M. Gerard, *Appl. Phys. Lett.* **78**, 2327 (2001).
- ¹⁷ P. Bhattacharya, X. H. Su, S. Chakrabarti, G. Ariyawansa, and A. G. U. Perera,

- Appl. Phys. Lett. **86**, 191106 (2005).
- ¹⁸ S. Raghavan, D. Forman, P. Hill, N. R. Weisse-Bernstein, G. von Winckel, P. Rotella, S. Krishna, S. W. Kennerly, and J. W. Little, J. Appl. Phys. **96**, 1036 (2004).
- ¹⁹ S. Kim, H. Mohesmi, M. Erdtmann, E. Michel, C. Jelen, and M. Razeghi, Appl. Phys. Lett. **73**, 963 (1998).
- ²⁰ J. Jiang, S. Tsao, T. O'Sullivan, W. Zhang, H. Lim, T. Sills, K. Mi, M. Razeghi, G. J. Brown, and M. Z. Tidrow, Appl. Phys. Lett. **84**, 2166 (2004).
- ²¹ J. Szafraniec, S. Tsao, W. Zhang, H. Lim, M. Taguchi, A. A. Quivy, B. Movaghar, and M. Razeghi, Appl. Phys. Lett. **88**, 121102 (2006).
- ²² E. Finkman, S. Maimon, V. Immer, G. Bahir, S. E. Schacham, F. Fossard, F. H. Julien, J. Brault, and M. Gendry, Phys. Rev. B **63**, 045323 (2001).
- ²³ L. Doyennette, L. Nevou, M. Tchernycheva, A. Lupu, F. Guillot, E. Monroy, R. Colombelli, and F. H. Julien, Electron. Lett. **41**, 1077 (2005).
- ²⁴ A. I. Yakimov, A. V. Dvurechenskii, A. I. Nikiforov, and Y. Y. Proskuryakov, J. Appl. Phys. **89**, 5676 (2001).
- ²⁵ P. Bhattacharya, S. Ghosh, and A. D. Stiff-Roberts, Annu. Rev. Mater. Res. **34**, 1 (2004).
- ²⁶ J.-Z. Zhang and I. Galbraith, Appl. Phys. Lett. **84**, 1934 (2004).
- ²⁷ H. Lim, W. Zhang, S. Tsao, T. Sills, J. Szafraniec, K. Mi, B. Movaghar, and M. Razeghi, Phys. Rev. B **72**, 085332 (2005).
- ²⁸ X. Han, J. Li, J. Wu, G. Cong, X. Liu, Q. Zhu, and Z. Wang, J. Appl. Phys. **98**, 053703 (2005).
- ²⁹ X. D. Jiang, S. S. Li, and M. Z. Tidrow, Physica E (Amsterdam) **5**, 27 (1999).
- ³⁰ V. G. Stoleru and E. Towe, Appl. Phys. Lett. **83**, 5026 (2003).
- ³¹ V. Ryzhii, Appl. Phys. Lett. **78**, 3346 (2001).
- ³² V. Ryzhii, I. Khmyrova, V. Mitin, M. Stroschio, and M. Willander, Appl. Phys. Lett. **78**, 3523 (2001).
- ³³ J. Phillips, J. Appl. Phys. **91**, 4590 (2002).
- ³⁴ V. Ryzhii, I. Khmyrova, V. Pipa, V. Mitin, and M. Willander, Semicond. Sci. Technol. **16**, 331 (2001).
- ³⁵ M. B. El Mashade, M. Ashry, and A. Nasr, Semicond. Sci. Technol. **18**, 891 (2003).
- ³⁶ V. Ryzhii, Semicond. Sci. Technol. **11**, 759 (1996).
- ³⁷ Y. Matsukura, Y. Uchiyama, R. Suzuki, T. Fujii, and N. Kajihara, Infrared Phys. Technol. **47**,

- 164 (2005).
- ³⁸ Z. Ikonić, P. Harrison, and R. W. Kelsall, *IEEE Trans. Electron Devices* **53**, 189 (2006).
- ³⁹ V. D. Jovanović, D. Indjin, N. Vukmirović, Z. Ikonić, P. Harrison, E. H. Linfield, H. Page, X. Marcadet, C. Sirtori, C. Worrall, et al., *Appl. Phys. Lett.* **86**, 211117 (2005).
- ⁴⁰ I. Savić, V. Milanović, N. Vukmirović, V. D. Jovanović, Z. Ikonić, D. Indjin, and P. Harrison, *J. Appl. Phys.* **98**, 084509 (2005).
- ⁴¹ V. D. Jovanović, P. Harrison, Z. Ikonić, and D. Indjin, *J. Appl. Phys.* **96**, 269 (2004).
- ⁴² T. B. Bahder, *Phys. Rev. B* **41**, 11992 (1990).
- ⁴³ B. Jogai, *J. Appl. Phys.* **88**, 5050 (2000).
- ⁴⁴ O. Stier, M. Grundmann, and D. Bimberg, *Phys. Rev. B* **59**, 5688 (1999).
- ⁴⁵ A. J. Davies, *The Finite Element Method* (Clarendon Press, Oxford, 1980).
- ⁴⁶ M. Tadić, F. M. Peeters, and K. L. Janssens, *Phys. Rev. B* **65**, 165333 (2002).
- ⁴⁷ N. Vukmirović, D. Indjin, V. D. Jovanović, Z. Ikonić, and P. Harrison, *Phys. Rev. B* **72**, 075356 (2005).
- ⁴⁸ U. Bockelman and G. Bastard, *Phys. Rev. B* **42**, 8947 (1990).
- ⁴⁹ T. Inoshita and H. Sakaki, *Phys. Rev. B* **56**, R4355 (1997).
- ⁵⁰ S. Hameau, Y. Guldner, O. Verzelen, R. Ferreira, G. Bastard, J. Zeman, A. Lemaître, and J. M. Gérard, *Phys. Rev. Lett.* **83**, 4152 (1999).
- ⁵¹ X.-Q. Li, H. Nakayama, and Y. Arakawa, *Phys. Rev. B* **59**, 5069 (1999).
- ⁵² O. Verzelen, R. Ferreira, and G. Bastard, *Phys. Rev. B* **62**, R4809 (2000).
- ⁵³ S. Sauvage and P. Boucaud, *Appl. Phys. Lett.* **88**, 063106 (2006).
- ⁵⁴ S. Sauvage, P. Boucaud, R. P. S. M. Lobo, F. Bras, G. Fishman, R. Prazeres, F. Glotin, J. M. Ortega, and J.-M. Gérard, *Phys. Rev. Lett.* **88**, 177402 (2002).
- ⁵⁵ E. A. Zibik, L. R. Wilson, R. P. Green, G. Bastard, R. Ferreira, P. J. Phillips, D. A. Carder, J.-P. R. Wells, J. W. Cockburn, M. S. Skolnick, et al., *Phys. Rev. B* **70**, 161305 (2004).
- ⁵⁶ N. Vukmirović, Z. Ikonić, V. D. Jovanović, D. Indjin, and P. Harrison, *IEEE J. Quantum Electron.* **41**, 1361 (2005).
- ⁵⁷ T. R. Nielsen, P. Gartner, and F. Jahnke, *Phys. Rev. B* **69**, 235314 (2004).
- ⁵⁸ J. Seebeck, T. R. Nielsen, P. Gartner, and F. Jahnke, *Phys. Rev. B* **71**, 125327 (2005).
- ⁵⁹ Z. Ikonić, V. Milanović, and M. Tadić, *J. Phys.: Condens. Matter* **7**, 7045 (1995).
- ⁶⁰ R. C. Iotti and F. Rossi, *Phys. Rev. Lett.* **87**, 146603 (2001).

- ⁶¹ I. Savić, Z. Ikonić, V. Milanović, N. Vukmirović, V. D. Jovanović, D. Indjin, and P. Harrison, Phys. Rev. B **73**, 075321 (2006).
- ⁶² L. R. C. Fonseca, J. L. Jimenez, J. P. Leburton, and R. M. Martin, Phys. Rev. B **57**, 4017 (1998).

Figure captions

FIG. 1: Schematic view of three QDIP periods: a) a realistic structure, b) the structure used in the modelling. The period of the structure in the growth direction z is equal to L_z .

FIG. 2: The effective potential profile on z -axis for the analyzed structure subjected to the electric field $F = 10$ kV/cm and the corresponding energy levels assigned to each of the five periods.

FIG. 3: The region of space in which the Hamiltonian eigenvalue problem is solved, consisting of $2N + 1$ periods ($N = 2$). The radius of the embedding cylinder is R_t and its length H_t . It is assumed that quantum dots have conical shape with diameter D and height h . The wetting layer width is d_{WL} .

FIG. 4: Quantum dot energy levels and the quantum number of the z -component of their total angular momentum at $F = 10$ kV/cm. According to their energy the states are grouped in five groups G_1 - G_5 .

FIG. 5: Calculated dependence of the dark current density on the electric field at the temperatures $T = 50$ K (circles), $T = 77$ K (squares) and $T = 100$ K (triangles). The inset gives a comparison of the experimental dark current results at $T = 77$ K (line) and calculated values (points).

FIG. 6: Occupancies of energy levels at three different values of electric field at a temperature of $T = 77$ K.

FIG. 7: The dependence of the average carrier transition rates from the states in groups G_2 to G_4 to the continuum (group G_5) on electric field at the temperatures $T = 50$ K (circles), $T = 77$ K (squares) and $T = 100$ K (triangles).

FIG. 8: The energy dependence of the optical matrix elements for absorption of z -polarized radiation from the ground state at an electric field of $F = 10$ kV/cm.

FIG. 9: The dependence of responsivity on the energy of photons of incident radiation at a temperature of $T = 77$ K and an electric field of $F = 7.5$ kV/cm (full line), $F = 10$ kV/cm (dashed line), $F = 15$ kV/cm (dashed-dotted line), and $F = 25$ kV/cm (dotted line).

FIG. 10: The dependence of responsivity on the energy of photons of incident radiation at the temperatures $T = 50$ K (full line), $T = 77$ K (dashed line) and $T = 100$ K (dashed-dotted line) and the values of electric field of $F = 10$ kV/cm (left) and $F = 25$ kV/cm (right).

FIG. 11: The change in the occupancies of energy levels due to the optical flux excitation of $\Phi = 10^{18}$ cm $^{-2}$ s $^{-1}$ at peak responsivity photon energy at three different values of electric

field and a temperature of $T = 77\text{ K}$. Only absolute values of the changes are presented and the negative (neg.) quantities are therefore marked.

Figures

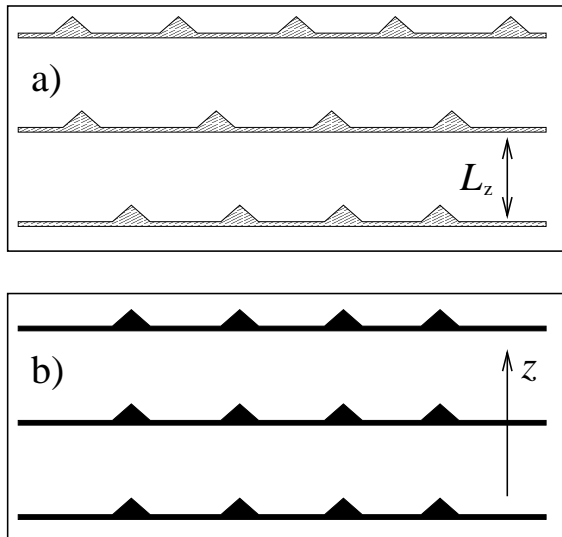


FIG. 1:

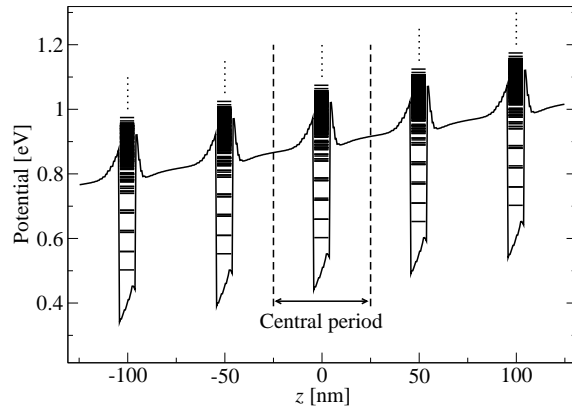


FIG. 2:

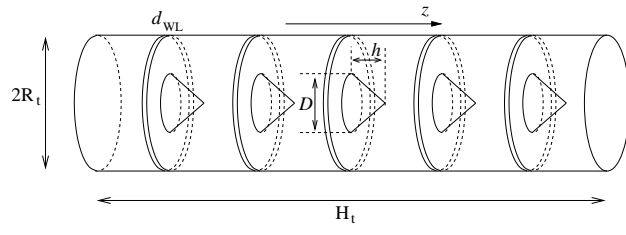


FIG. 3:

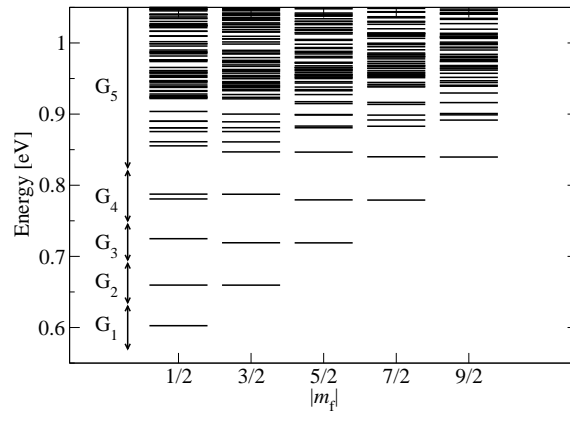


FIG. 4:

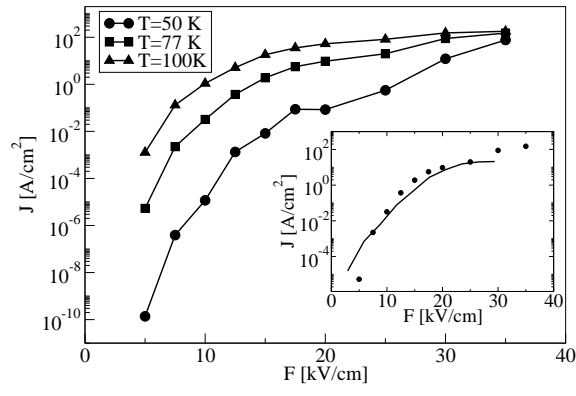


FIG. 5:

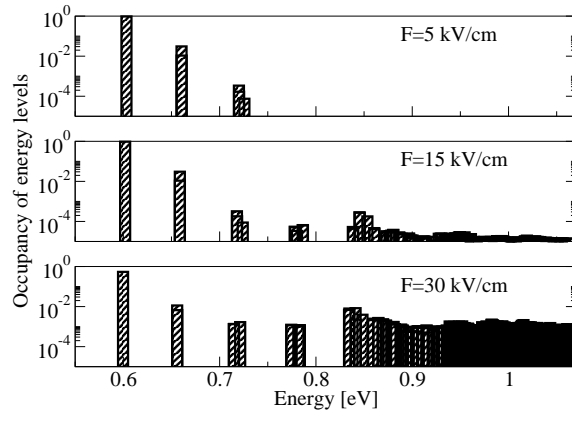


FIG. 6:

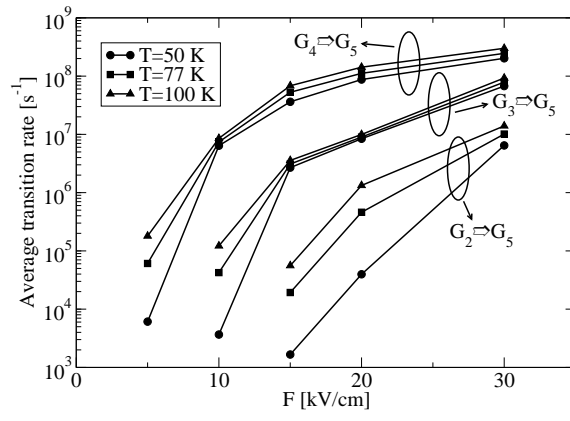


FIG. 7:

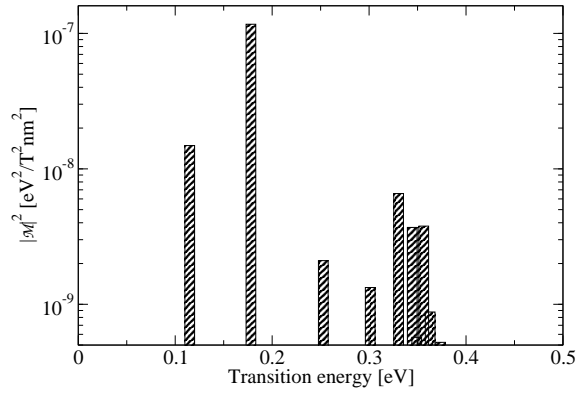


FIG. 8:

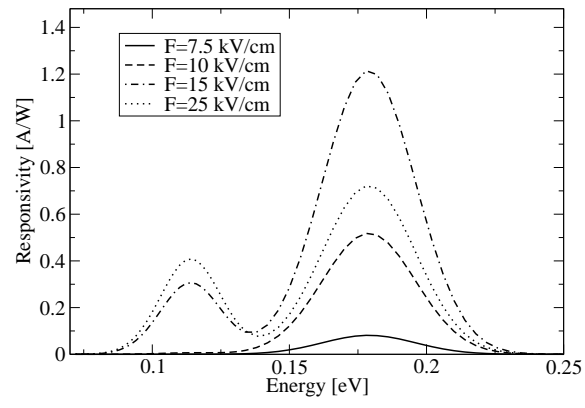


FIG. 9:

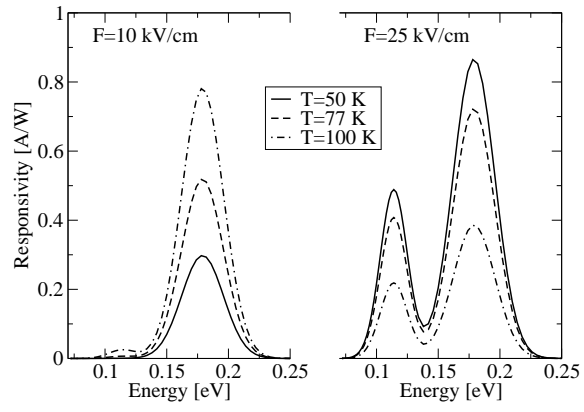


FIG. 10:

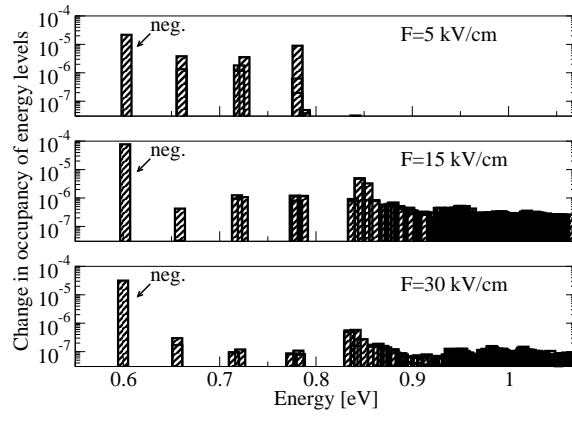


FIG. 11: